Molecular Dynamics–Continuum Hybrid Simulation for the Impingement of Droplet on a Liquid Film

Wen-Jing Zhou[a], Zhi-Qiang Yu[a], Zhong-Zhen Li[a], Ya-Ling He[a] & Wen-Quan Tao[a]

[a] Key Laboratory of Thermo-Fluid Science and Engineering of MOE, School of Energy and Power Engineering, Xi'an Jiaotong University, Xi'an, Shaanxi, People's Republic of China
Published online: 23 Apr 2015.

Click for updates

PLEASE SCROLL DOWN FOR ARTICLE

Taylor & Francis
Taylor & Francis Group

MOLECULAR DYNAMICS–CONTINUUM HYBRID SIMULATION FOR THE IMPINGEMENT OF DROPLET ON A LIQUID FILM

Wen-Jing Zhou, Zhi-Qiang Yu, Zhong-Zhen Li, Ya-Ling He, and Wen-Quan Tao

Key Laboratory of Thermo-Fluid Science and Engineering of MOE, School of Energy and Power Engineering, Xi'an Jiaotong University, Xi'an, Shaanxi, People's Republic of China

A molecular dynamics–continuum hybrid method is used to study the droplet impingement process on a liquid film. The hybrid code is validated by simulating the sudden-start Couette flow and unsteady heat transfer problem. The impingement process is strongly affected by Weber number. At low Weber number, the evolution of the crown after droplet impingement is stable, while at high Weber number the secondary droplets emerge and the splash phenomenon occurs. The effect of liquid film thickness on the evolution of crown diameter is also investigated.

1. INTRODUCTION

Impingement of droplets on liquid film is an important process in many applications, including ink-jet printing, spray cooling, and spray combustion in an internal combustion engine, as well as corrosion of turbine blades. The process of the droplet impingement on a liquid film is affected by a large number of factors, including both dimensionless criteria such as Weber number (the ratio of inertia to surface tension forces) and dimensional quantities such as the droplet diameter, droplet velocity, impact angle, and thickness of liquid film. These factors have been studied both experimentally and numerically in recent decades. Manzello and Yang [1] experimentally studied water droplet impingement on a liquid surface of varying impact velocity and liquid depth. They found that the critical impact Weber number for jet breakup was independent of liquid depth. It has been determined that on the way to the liquid surface, both coalescence and jetting of droplets are possible. Zhao et al. [2] experimentally investigated the transition between coalescence and jetting when droplets of different density, viscosity, and surface tension impinged on a deep liquid pool. It was concluded that the instability during impact processes can be

Color versions of one or more of the figures in the article can be found online at www.tandfonline.com/unht.

NOMENCLATURE

c_p	specific heat	$\triangle x, \triangle z$	grid size in x, z directions
D	diameter of droplet	δ	liquid film thickness
H	channel height	δt	time step
l	length	ϵ	characteristic energy
$L1$	maximum number of grids in x direction	λ	thermal conductivity
m	atom mass	μ	dynamic viscosity
$M1$	maximum number of grids in z direction	ρ	density
N	number of meshes	σ	characteristic length, surface tension
p	pressure	ϕ	potential function
r	atom distance		
$\mathbf{r}$	position vector	**Subscripts**	
t	time	c	cutoff, crown
T	temperature	h	high temperature
u, w	velocity component in x, z directions	l	low temperature
$\mathbf{u}$	velocity vector	w	wall
U	wall velocity, impact velocity of droplet	**Superscripts**	
We	Weber number	C	C region
x, y, z	Cartesian coordinates	P	P region
$\triangle n$	change of atom number	wf	related to wall–fluid interaction
		*	dimensionless value
		–	mean value

increased by reducing viscosity and low surface tension. The effects of liquid depth, as well as fluid surface tension and viscosity, on the drop–surface behavior were studied experimentally [3]. Experimental, numerical, and theoretical investigations were conducted by Berberović et al. [4] to study the dynamics of droplet impact on a liquid surface. The effects of certain parameters, including droplet impact velocity, liquid film thickness, liquid viscosity, and surface tension, were studied in their investigation. It was demonstrated that after the impingement of droplets on a liquid film, a very complicated breakage of local liquid film may occur, and an ascending crown may be formed. A level set method was used in [5] for tracking the interface during droplet impaction on liquid film. For the early stage of crown formation, this method could well predict the process characteristics. Xie et al. [6] numerically simulated the process of droplet impact on a liquid surface using the moving particle semi-implicit method. They found that the liquid depth and the droplet velocity can markedly affect the dynamic processes, and the change in the crown radius over time can be described by a square function.

From this brief review of the literature, it can be concluded that the dynamics of droplet impact on a liquid surface is very complicated and has been widely investigated, and the influences of many factors such as droplet diameter, droplet velocity, and the liquid film thickness have also been studied. However, all studies mentioned above were performed at the macroscale level, and to the authors' knowledge few studies have been reported on droplet impact phenomena at the nanoscale level. Molecular dynamics (MD) simulation is an appropriate tool to perform simulation at such a scale. The most important feature of MD simulation is that we do not need to track interfaces by using macro interface-tracking methods such as level set since

interfaces are directly generated. Moreover, MD simulation can provide us with details that are difficult to capture experimentally. Nevertheless, MD simulations are very time-consuming, and they often require massive computer memory. In this regard, the hybrid MD–continuum methods developed recently [7–14] provide a feasible way to realize such a simulation. In such hybrid methods, MD is used to obtain atomistic information in the interface region, while continuum methods such as the finite volume method (FVM) and lattice Boltzmann Method (LBM) are used to solve Navier–Stokes (NS) equations in the remaining part of the computational region. Information exchanges are executed in the overlap region where the two methods are both valid and used.

The remainder of the article is outlined as follows: In Section 2, the hybrid method is briefly introduced. In Section 3, the hybrid method is validated, and the results of droplet impingement on liquid film are presented. Finally, some remarks are presented in Section 4.

2. HYBRID METHOD

2.1. Domain Decomposition

The schematic of droplet impingement on the liquid film is shown in Figure 1. The droplet is placed on the center line of the computational domain above the liquid film, which is supported by a solid wall. The liquid film can be divided into two parts: the upper part is simulated by MD, while FVM is used for the lower part to conserve computing resources. The details of coupling between MD and FVM can be found in Figure 2. The region containing the droplet and part of the liquid film is called the P (particle) region, where droplet impingement takes place. The remaining part is referred to as the C (continuum) region, in which the NS equations can be used to describe the fluid flow behavior. To ensure the information exchange between the P and C regions, there should be an intervening overlap (O) region. In the O region, both MD and FVM are valid and employed.
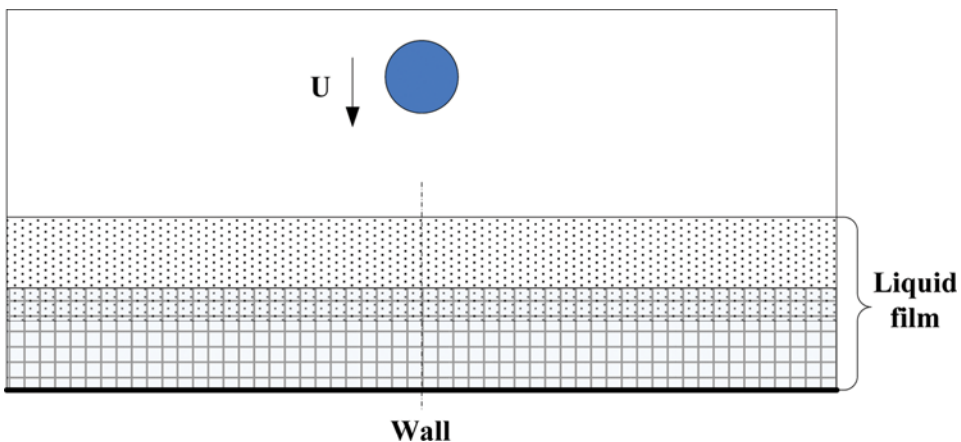

Figure 1. Schematic of droplet impingement on liquid film.
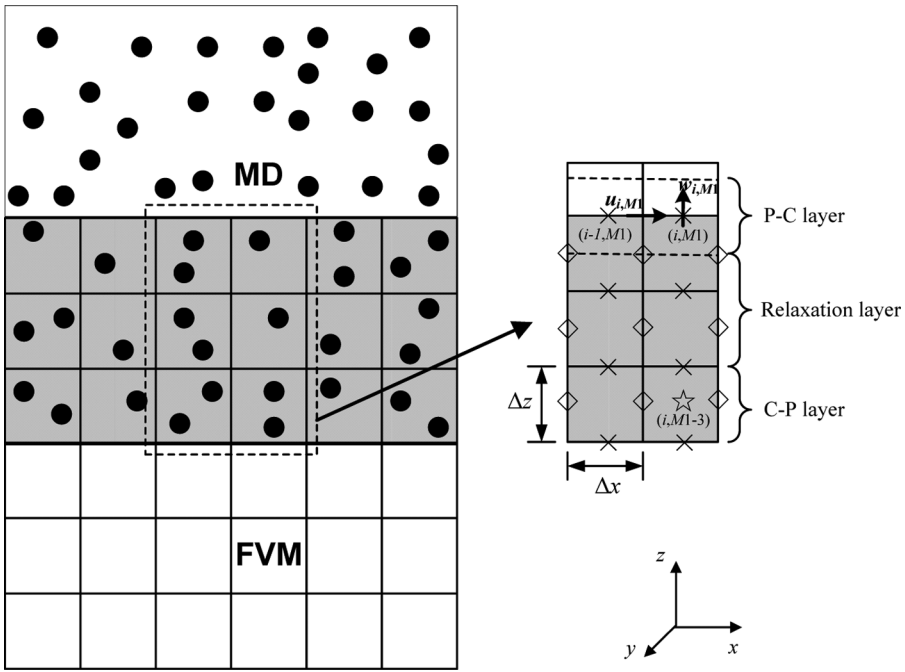
Figure 2. Schematic diagram of domain decomposition.

2.2. Molecular Dynamics Simulation

The flow characteristics of the droplet and part of the liquid film are predicted by MD simulation. The diameter of the droplet is 12 nm and is placed 4 nm above the liquid film. The thickness of liquid film for MD is fixed at 60 nm, while that for FVM ranges from 40 to 80 nm. Thus, the total thickness of the liquid film varies from 92 to 132 nm (allowing 8 nm for O region), resulting in different grid numbers in the z direction for FVM. The domain size for the other two directions is $l_x^P \times l_y^P = 180$ nm $\times$ 2 nm. To describe the atomic interaction, the following Lennard–Jones potential is used:

$$\phi(r) = 4\varepsilon\left[\left(\frac{\sigma}{r}\right)^{12} - \left(\frac{\sigma}{r}\right)^6\right] \tag{1}$$

where $\epsilon = 1.67 \times 10^{-21}$ J and $\sigma = 0.341$ nm are the energy and length characteristic parameters, respectively, for argon. When the distance between atoms is larger than r_c, which is selected as 1.0 nm, interactions among atoms are ignored. Newton's equation of motion is used to update the atom acceleration:

$$m_i\frac{d^2\mathbf{r}_i}{dt^2} = -\sum_{j\neq i}\frac{\partial\phi_{ji}}{\partial\mathbf{r}_i} \tag{2}$$

where m_i is the mass of argon atoms. The Verlet velocity algorithm with a time step δt^P of 0.005 ps is used to integrate the Newton's equations of motion. All

MD simulations are performed using the large-scale atomic/molecular massively parallel simulator (LAMMPS) [15].

The droplet and liquid film are both composed of argon atoms of the same density (1,378.28 kg/m³), which corresponds to the saturated liquid density at temperature $T = 89.85$ K that is adopted as the initial system temperature. At this temperature, the droplet is surrounded by argon vapor at a saturated vapor density 7.47 kg/m³. Even though a three-dimensional (3D) system is used in MD simulation, the droplet impingement problem is actually 2D in the present article since periodic boundaries are used in both x and y directions. In regard to the z direction, a specular wall is used at the top of the P region to avoid atoms drifting away from the system. Whenever an atom arrives at the top boundary, it will be reflected back into the system with the direction of the normal velocity vector reversed.

2.3. Finite-Volume Method

FVM is adopted as the continuum solver in the C region for 2D incompressible NS equations [16]:

$$\nabla \cdot \mathbf{u} = 0 \tag{3}$$

$$\frac{\partial \mathbf{u}}{\partial t} + \mathbf{u} \cdot \nabla \mathbf{u} = \frac{\mu}{\rho} \nabla^2 \mathbf{u} - \frac{1}{\rho} \nabla p \tag{4}$$

$$\frac{\partial T}{\partial t} + \mathbf{u} \cdot \nabla T = \frac{\lambda}{\rho c_p} \nabla^2 T + \frac{2\mu}{\rho c_p} \left[\left(\frac{\partial u}{\partial x}\right)^2 + \left(\frac{\partial w}{\partial z}\right)^2 + \frac{1}{2} \left(\frac{\partial u}{\partial z} + \frac{\partial w}{\partial x}\right)^2 \right] \tag{5}$$

where u and w are velocity in the x and z directions, respectively, and μ, c_p, and λ are the dynamic viscosity, specific heat, and thermal conductivity, respectively. These coefficients are available in the fluid database [17], and their values are $\mu = 249.2$ uPa · s, $c_p = 1,120.8$ J · kg⁻¹ · K⁻¹, and $\lambda = 0.1223$ W · m⁻¹ · K⁻¹, respectively, which correspond to the liquid state of $\rho = 1,378.28$ kg/m³ and $T = 89.85$ K. During the droplet impingement process, the temperature of the C region changed little while the solid wall had a fixed temperature $T_w = 89.85$ K, and thus we use the coefficients at $T = 89.85$ K.

The semi-implicit method for pressure-linked equations consistent (SIMPLEC) algorithm [16] is adopted to obtain the numerical solutions of NS equations. To study the effect of different depths of liquid film, we use three different sizes in the z direction for the C region, namely, $l_z^C = 40$, 60, and 80 nm. Because of the symmetry in the x (i.e., horizontal) direction, only half of the bottom part of the liquid film (Figure 1) needs to be studied by FVM; the left half was chosen. Therefore, the C region is divided by meshes of $N_x^C \times N_z^C = 50 \times 20$, 50×30, and 50×40 for the three cases, with a grid size $\Delta x = 1.8$ nm and $\Delta z = 2$ nm. The time step for the C region is $\delta t^C = 50 \delta t^P = 0.25$ ps. A staggered grid is used, requiring that velocities u and w be located at the faces of the main control volumes, while the other quantities including pressure, density, and temperature are defined at the center of the main control volumes. As shown in Figure 2, velocities u and w are denoted by diamonds and

crosses, respectively. The boundary conditions for the C region are as follows: left and right boundaries are symmetric, which means $\left(\frac{\partial w}{\partial x}\right)_{0,j} = \left(\frac{\partial T}{\partial x}\right)_{0,j} = 0$, $u_{1,\ j} = 0$, and $\left(\frac{\partial w}{\partial x}\right)_{L1,j} = \left(\frac{\partial T}{\partial x}\right)_{L1,j} = 0$, $u_{L1,\ j} = 0$; the bottom boundary is solid wall with no velocity slip or temperature jump; the top boundary is the P–C boundary, where the macroscopic quantities (u, w, and T) at the boundary are averaged from the information obtained by MD in the P region.

2.4. Coupling Scheme

As shown in Figure 2, the O region can be divided into three parts: P–C layer, relaxation layer, and C–P layer. The horizontal center line of the P–C layer coincides with the top boundary of the C region, so the averaged quantities within the P–C layer such as u, w, and T are applied directly to the C region as its boundary condition. Note that the areas used for gathering information on velocities u and w for the top boundary of the C region have an offset of $\Delta x/2$ in the x direction because of the staggered character of the grid system. Restriction on atoms for momentum and energy coupling is realized in the C–P layer. For momentum coupling, we use the formula proposed by Nie et al. [10] and later enhanced by Yen et al. [18]. Taking the grid (i, $M1 - 3$), for example, the formula is

$$\ddot{\mathbf{r}}_i(t) = \frac{1}{(p/2 + 1)\delta t^{\mathrm{P}}} \left[\mathbf{u}_{i,M1-3}(t + \delta t^{\mathrm{P}}) - \left\langle \frac{1}{N^{\mathrm{C-P}}} \sum_{j=1}^{N^{\mathrm{C-P}}} \dot{\mathbf{r}}_j(t) \right\rangle_{p\delta t^{\mathrm{P}}} \right]$$
$$+ \left[\frac{\mathbf{f}_i(t)}{m} - \left\langle \frac{1}{N^{\mathrm{C-P}}} \sum_{j=1}^{N^{\mathrm{C-P}}} \frac{\mathbf{f}_j(t)}{m} \right\rangle_{p\delta t^{\mathrm{P}}} \right] \qquad (6)$$

where $\mathbf{u}_{i,M1-3}(t + \delta t^P)$ is the velocity vector at the center of the grid (i, $M1 - 3$), $p = 50$, $\langle \rangle_{p\delta t^P}$ is the value averaged from $t - p\delta t^{\mathrm{P}}$ to t, which corresponds to the middle time instant ($t - p\delta t^{\mathrm{P}}/2$), and $N^{\mathrm{C-P}}$ represents the number of atoms in the C–P layer, i.e., the grid (i, $M1 - 3$). The left-hand term of Eq. (6) represents the revised acceleration of particle i; the first term in the first square bracket on the right-hand side is the target velocity; the second term in this bracket is the averaged velocity in the C–P layer; and the first term in the second square bracket denotes the force exerted on particle i from other particles; the second term in this bracket represents the averaged force in the C–P layer. Following such modification, the distribution of particle velocities will be consistent with the macroscopic velocity in the C–P layer.

For energy coupling, the velocity rescaling method [19, 20] is used:

$$\mathbf{u}_i = \bar{\mathbf{u}} + \sqrt{\frac{T_{i,M1-3}}{T_{MD}^{C-P}}}(\mathbf{u}_i - \bar{\mathbf{u}}) \qquad (7)$$

where $\bar{\mathbf{u}}$ is the mean velocity of atoms in the C–P layer, $T_{i,M1-3}$ is the temperature at the center of the grid (i, $M1 - 3$) from the continuum solutions, and $T_{\mathrm{MD}}^{\mathrm{C-P}}$ is the atomic temperature in the C–P layer. The velocity rescaling method should be used on thermal velocities after the mean velocity $\bar{\mathbf{u}}$ is removed.

To ensure mass conservation, atoms are removed or added near the lower boundary of the C–P layer according to the continuum velocities at the boundary. Taking the grid $(i, M1 - 3)$, for example, during a single time step δt^C in the C region, the change in the number of atoms in the MD cell corresponding to the grid $(i, M1 - 3)$ is [20]:

$$\Delta n = \Delta x l_y^P \rho w_{i,M1-3} \delta t^C / m \tag{8}$$

where $\triangle x$ and l_y^P are the grid size $(i, M1 - 3)$ in the x direction and the size of the P region in the y direction, respectively, so $\Delta x l_y^P$ is the area of the surface through which atoms enter or leave the cell. $w_{i,M1-3}$ is the z component of the velocity at the southern boundary of the grid $(i, M1 - 3)$ and m is the mass of atoms. If the change in the number of atoms in Eq. (8) is smaller than 1, it will be added to the next time step δt^C. When the magnitude of the accumulated number n_0 is larger than 1, we choose the nearest integer n_I of this number, and the magnitude of n_I should be smaller than that of n_0. If n_I is negative, $-n_I$ atoms closest to the boundary are removed. If the flux is positive, n_I atoms are inserted during the period of the following δt^C, with an appropriate temporal interval to ensure that n_I atoms are evenly distributed. The fractional reminder $n_0 - n_I$ will be added to the next δt^C. In regard to atom insertion the USHER algorithm [21] is used because of its feasibility for dense fluids.

3. RESULTS AND DISCUSSION

3.1. Code Validation

The problem of sudden-start Couette flow and unsteady heat transfer is studied in this section to validate our hybrid codes. For sudden-start Couette flow, geometric size in the z direction of the system is set identical to that in Ref. [10]. The height H of the channel is 17.714 nm. As shown in Figure 3, from $z = 0$ to $z = 10.642$ nm, MD
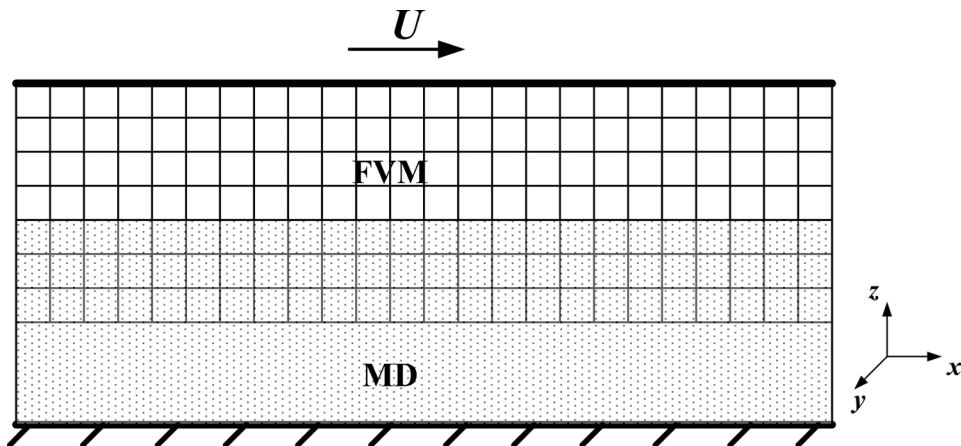

Figure 3. Schematic of sudden-start Couette flow and unsteady heat transfer.

simulation is used; from $z = 5.304$ to $z = 17.714$ nm, FVM is employed. Thus, the overlap region is from $z = 5.304$ to $z = 10.642$ nm, and it contains three FVM grids. The size in the other two directions is $l_x = 21$ and $l_y = 17.1$ nm, respectively. Periodic boundary conditions are imposed at the four boundaries in the x and y directions. The density and temperature of liquid confined between two walls are the same as that of droplet and liquid film in the droplet impingement problem (i.e., $\rho = 1{,}378.28$ kg/m^3, $T = 89.85$ K). The temperature of liquid in the y direction is fixed using a Langevin thermostat [22]. No-slip boundary conditions are set for the upper wall in FVM. Two layers of atoms of face-centered cubic (1 1 1) structure are used to construct the lower wall. The parameters for the interactions between the wall and liquid atoms are set as $\varepsilon^{wf} = 0.6\varepsilon$ and $\sigma^{wf} = \sigma$ in order to impose a non-slip boundary condition at the lower wall [7].

　　The initial mean velocity of all atoms is zero. Before Couette flow starts, the system runs 100,000 time steps in order to reach the thermal equilibrium. Then at $t = 0$, the velocity of the upper wall changes to $U = 157.6$ m/s while the lower wall remains stationary. Figure 4 shows the velocity profiles at different times. Triangles and squares represent the results from MD and FVM, respectively, while the analytical solutions are indicated by lines. It can be seen that the hybrid results agree well with the analytical solutions for different time intervals, validating the correctness of the momentum coupling in the overlap region.

　　In regard to the unsteady heat transfer problem, the height H of the channel is increased to 26.5 nm. MD simulation is used in two subdomains near the upper ($15.9 \leq z \leq 26.5$ nm) and lower walls ($0 \leq z \leq 10.6$ nm), while FVM is used in the central region ($5.3 \leq z \leq 21.2$ nm). The parameters for interactions between the wall and liquid atoms are set as $\varepsilon^{wf} = 1.5\varepsilon$ and $\sigma^{wf} = \sigma$ for both walls in order to reduce the temperature jump there. Before the unsteady heat transfer starts, the system runs
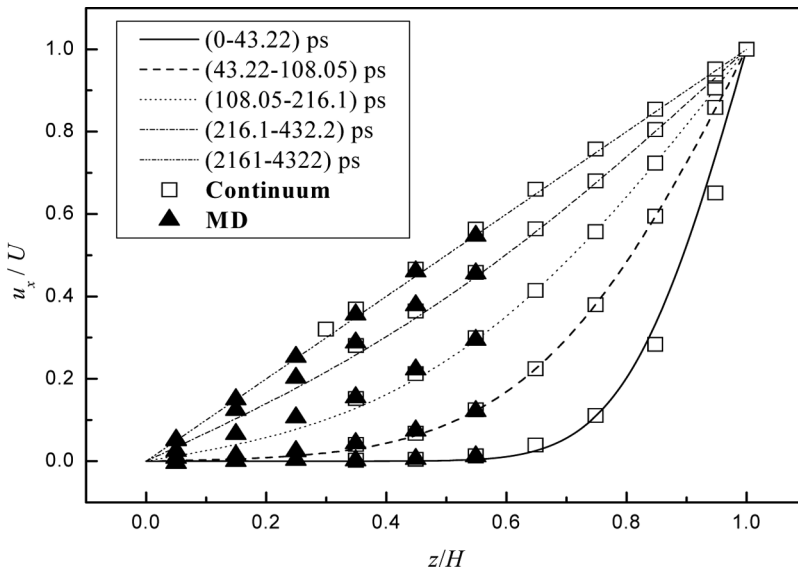

Figure 4. Velocity profiles at different times in sudden-start Couette flow.

100,000 time steps in order to reach the thermal equilibrium at 90 K. Then at $t = 0$, the temperature of the upper wall changes to $T_h = 110$ K while that of the lower wall is $T_l = 90$ K. In regard to this problem, there are still minor temperature jumps at the walls, although the energy parameter ε^{wf} is increased to 1.5ε, so analytical solutions are not available without exact boundary conditions. To validate the hybrid code, the results from pure MD simulations are needed. Figure 5 shows the temperature profiles at different times. Triangles and squares represent hybrid results, while pure MD results are shown by lines. The good agreement between hybrid results and pure MD results at different time intervals indicates the correctness of the energy coupling in the overlap region.

3.2. Hybrid Results for Impingement of Droplet on Liquid Film

In this section, our hybrid code is employed to investigate the droplet impingement process on liquid film. Initially, the droplet is placed 4 nm above the liquid film. Before the impingement starts, the system runs 50,000 time steps in order to reach the thermal equilibrium. At such small scales, the effect of gravity can be ignored, so the position of the droplet remains unchanged during the thermal equilibrium period. A velocity within the range 300–700 m/s is then imposed on the droplet in the z direction. After a short time, the droplet reaches the surface of the liquid film and the impingement starts.

In order to compare our results to those of others at different scales, nondimensional numbers are used: Weber number $\mathrm{We} = \rho U^2 D / \sigma$; dimensionless liquid film thickness $\delta = H/D$; dimensionless time $t^* = tU/D$. In these expressions, ρ and σ denote the density and surface tension of the droplet and liquid film, U is the droplet impact velocity, D is the droplet diameter, H is the initial liquid film thickness, and t is time. The surface tension σ of the liquid used in the present article can be obtained from The National Institute of Standards and Technology (NIST) of USA [17] or other MD simulations [23], and its value here is taken as 0.012 N/m.
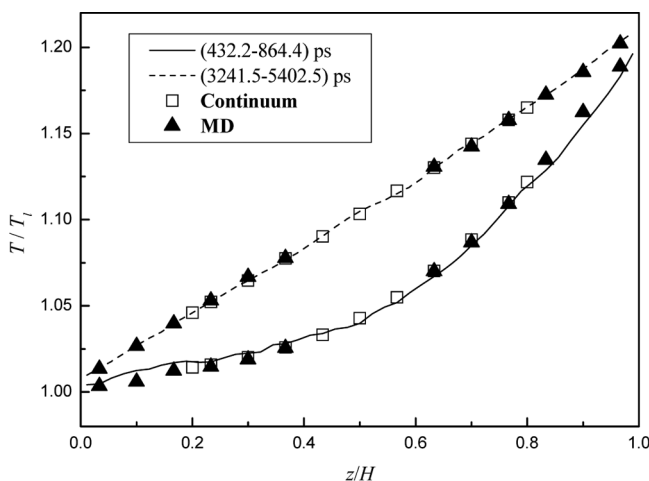

Figure 5. Temperature profiles at different times in unsteady heat transfer.

Figure 6 shows the time evolution of the droplet impingement process with an initial velocity of 700 m/s, We = 675, and δ = 7.67. The moment when the droplet reaches the liquid surface is considered as $t = 0$. Immediately after impact, a small liquid jet emerges on the liquid surface and spreads upward and outward, then a crater is formed in the liquid film with its shape changing from oblate to circular. The downward expansion of this crater forces the liquid between that and the solid wall to move downward and is then repelled by the wall which thus presses the liquid on both sides of the crater to move upward. Consequently, the height of the liquid surface increases. Figure 7 shows the velocity vectors at $t = 531.25$ ps at the later stage of the droplet impingement process. It will clearly be seen that the liquid below the crater flows downward and changes its velocity direction when it arrives at the wall. Two vortices are found on both sides of the crater. This result is consistent with that found in Ref. [4].

It can be seen in Figure 6d that as the crown spreads outward two secondary droplets emerge, separate themselves from the crown, and then evaporate. Figure 6e shows that another, larger secondary droplet emerges and separates itself from the crown some time later. This secondary droplet has such a large velocity that it keeps moving upward in the vapor phase. Since the gravity effect can be ignored at such a small scale, this secondary droplet will not descend and merge into the liquid film. For comparison, Figure 8 shows the time evolution of the droplet impingement process with an initial velocity of 300 m/s, We = 124, and δ = 7.67. There is no generation of a secondary droplet during the entire process due to the low We number.

The evolution of the crown diameter D_c after impingement for two different Weber numbers (We = 675 and We = 496) is shown in Figure 9. These two Weber numbers correspond to the impact velocity of $U = 700$ and $U = 600$ m/s, respectively. The numerical results are compared to the experimental results of Cossali et al. [24],
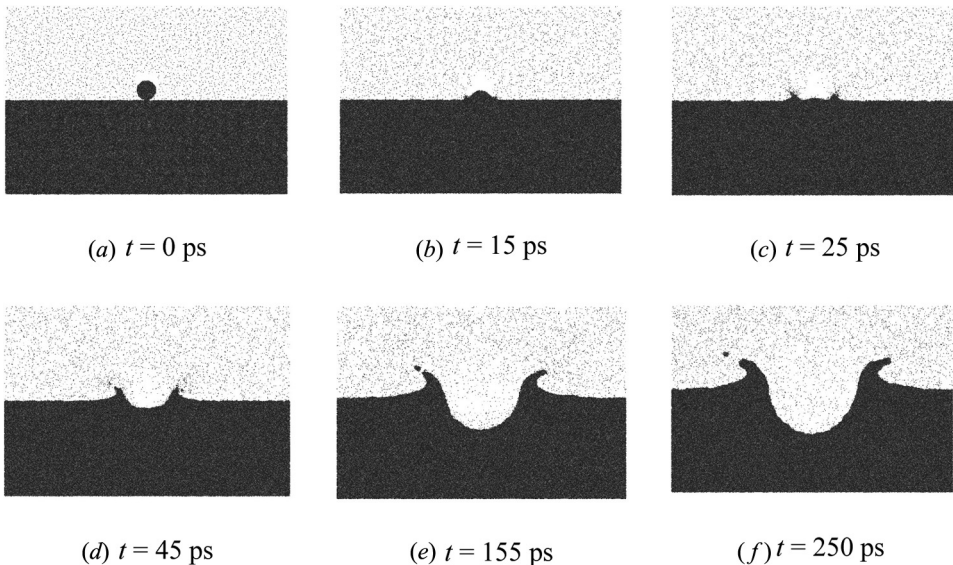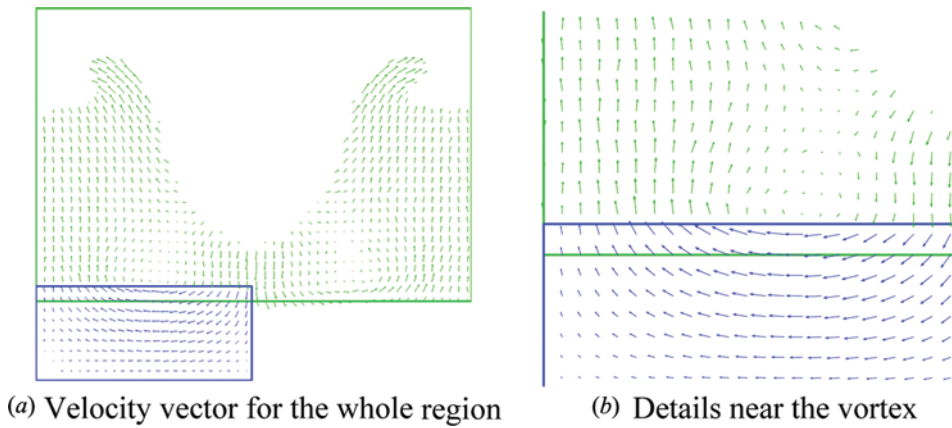

(a) $t = 0$ ps   (b) $t = 15$ ps   (c) $t = 25$ ps

(d) $t = 45$ ps   (e) $t = 155$ ps   (f) $t = 250$ ps

Figure 6. Time evolution of droplet impingement process with an initial velocity 700 m/s.

(a) Velocity vector for the whole region   (b) Details near the vortex

Figure 7. Velocity vectors at $t = 531.25$ ps for initial velocity of 700 m/s.

from which the results of two relatively close Weber numbers (667 and 484) and the largest dimensionless liquid film thickness ($\delta = 1.13$) are chosen. Although the change trends are the same: the dimensionless diameter increases with time but the rate of increase decreases with time, and the dimensionless diameters at different dimensionless time from our simulation are almost twofold those of the experimental data. This infers that the spread speed of the crown after droplet impingement at the nanoscale is greater than that at the microscale, based on the fact that the droplet diameter here is 12 nm as opposed to 3.82 mm in Ref. [24]. This difference may have been caused by variation in dimensionless liquid film thickness. In our simulation $\delta = 7.67$, while the dimensionless liquid film thickness chosen from [24] is $\delta = 1.13$. When the liquid film thickness decreases, the friction effect from the wall increases and impedes the spread of the crown, which was also found by Lee et al. [5].

The effect of liquid film thickness on the evolution of D_c/D is also studied for the case of We $= 675$. As shown in Figure 10, at the early stage of the impingement

(a) $t = 0$ ps   (b) $t = 25$ ps   (c) $t = 155$ ps

(d) $t = 250$ ps   (e) $t = 350$ ps   (f) $t = 450$ ps
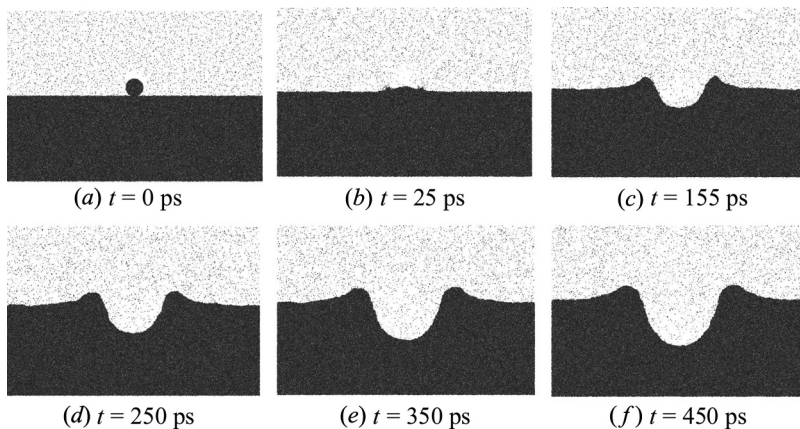
Figure 8. Time evolution of the droplet impingement process with initial velocity 300 m/s.
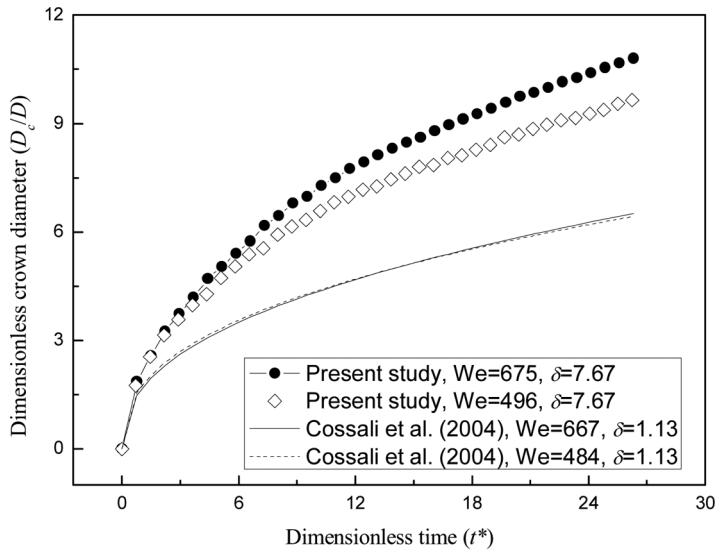
Figure 9. Crown diameter evolution at various Weber numbers.

process, the effect of liquid film thickness seems marginal. With the increase in time, this effect is gradually identified and when $t^* \approx 8$, the differences become obvious. However, variation in D_c/D versus t^* is not monotonic: for a given time when δ equals 7.67 and 9.33, the crown diameter is the smallest and largest, respectively, with that for $\delta = 11$ being somewhere in between. It seems that there is a value of δ which results in the largest crown diameter at the same t^*.
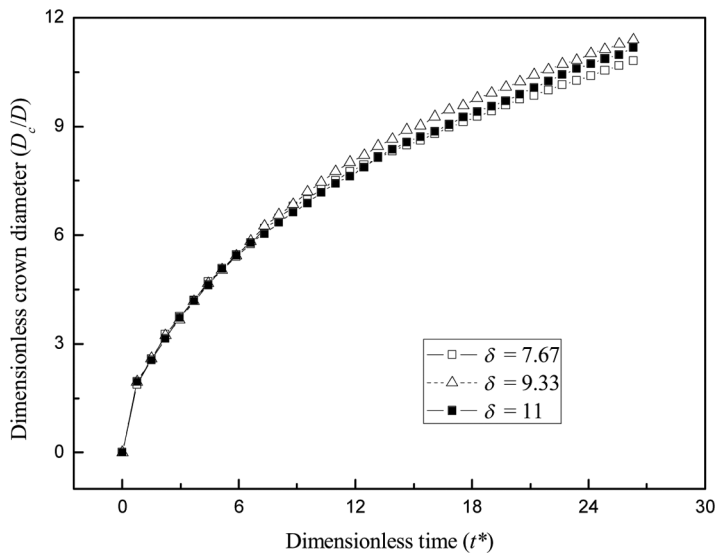

Figure 10. Crown diameter evolution at various dimensionless liquid film thicknesses (We = 675).

4. CONCLUSION

A MD–continuum hybrid method is used to investigate the droplet impingement process on a liquid film. The hybrid method is validated by sudden-start Couette flow and the unsteady heat transfer problem. The results of the hybrid method agree well with analytical solutions and pure MD results.

It is found that the droplet impingement process is sensitive to Weber number: when Weber number is low, the evolution of the crown is stable; when Weber number is high, secondary droplets emerge at the edge of the crown and then separate themselves from it, resulting in the splash phenomenon. At the later stage of the droplet impingement process, vortices are found in the liquid film.

The dimensionless crown diameters for different Weber numbers recorded by our hybrid method are of the same order of magnitude as the experimental data. Because of greater dimensionless liquid film thickness, crown spread was faster in our study than that observed experimentally. Finally, by investigating the effect of liquid film thickness, it is concluded that there is a particular value of dimensionless liquid film thickness that can produce the largest crown diameter.

REFERENCES

1. S. L. Manzello and J. C. Yang, An Experimental Study of a Water Droplet Impinging on a Liquid Surface, *Exp. Fluids*, vol. 32, no. 5, pp. 580–589, 2002.
2. H. Zhao, A. Brunsvold, and S. Munkejord, Investigation of Droplets Impinging on a Deep Pool: Transition from Coalescence to Jetting, *Exp. Fluids*, vol. 50, no. 3, pp. 621–635, 2011.
3. R. Vander Wal, G. Berger, and S. Mozes, Droplets Splashing upon Films of the Same Fluid of Various Depths, *Exp. Fluids*, vol. 40, no. 1, pp. 33–52, 2006.
4. E. Berberović, N. P. van Hinsberg, S. Jakirlić, I. V. Roisman, and C. Tropea, Drop Impact onto a Liquid Layer of Finite Thickness: Dynamics of the Cavity Evolution, *Phys. Rev. E*, vol. 79, no. 3, pp. 036306, 2009.
5. S. Lee, N. Hur, and S. Kang, A Numerical Analysis of Drop Impact on Liquid Film by Using a Level Set Method, *J. Mech. Sci. Technol.*, vol. 25, no. 10, pp. 2567–2572, 2011.
6. H. Xie, S. Koshizuka, and Y. Oka, Modelling of a Single Drop Impact onto Liquid Film Using Particle Method, *Int. J. Numer. Methods Fluids*, vol. 45, no. 9, pp. 1009–1023, 2004.
7. S. T. O'Connell and P. A. Thompson, Molecular Dynamics–Continuum Hybrid Computations: A Tool for Studying Complex Fluid Flows, *Phys. Rev. E*, vol. 52, no. 6, pp. R5792–R5795, 1995.
8. E. G. Flekkøy, G. Wagner, and J. Feder, Hybrid Model for Combined Particle and Continuum Dynamics, *Europhys. Lett.*, vol. 52, no. 3, pp. 271, 2000.
9. R. Delgado-Buscalioni and P. V. Coveney, Continuum-Particle Hybrid Coupling for Mass, Momentum, and Energy Transfers in Unsteady Fluid Flow, *Phys. Rev. E*, vol. 67, no. 4, pp. 046704, 2003.
10. X. B. Nie, S. Y. Chen, E. Weinan, and M. O. Robbins, A Continuum and Molecular Dynamics Hybrid Method for Micro- and Nano-Fluid Flow, *J. Fluid Mech.*, vol. 500, pp. 55–64, 2004.

11. W. Q. Tao and Y. L. He, Recent Advances in Multiscale Simulations of Heat Transfer and Fluid Flow Problems, *Prog. Comput. Fluid Dyn.*, vol. 9, no. 3, pp. 150–157, 2009.

12. J. Sun, Y. L. He, and W. Q. Tao, Scale Effect on Flow and Thermal Boundaries in Micro-/Nano-Channel Flow Using Molecular Dynamics–Continuum Hybrid Simulation Method, *Int. J. Numer. Methods Eng.*, vol. 81, no. 2, pp. 207–228, 2010.

13. Y. L. He and W. Q. Tao, Multiscale Simulations of Heat Transfer and Fluid Flow Problems, *ASME J. Heat Transfer*, vol. 134, no. 3, pp. 031018, 2012.

14. W. J. Zhou, H. B. Luan, J. Sun, Y. L. He, and W. Q. Tao, A Molecular Dynamics and Lattice Boltzmann Multiscale Simulation for Dense Fluid Flows, *Numer. Heat Transfer B Fundam.*, vol. 61, no. 5, pp. 369–386, 2012.

15. S. Plimpton, Fast Parallel Algorithms for Short-Range Molecular Dynamics, *J. Comput. Phys.*, vol. 117, no. 1, pp. 1–19, 1995.

16. W. Q. Tao, *Numerical Heat Transfer*, 2nd ed., Xi'an Jiaotong University Press, Xi'an, 2001.

17. E. W. Lemmon, M. O. McLinden, and D. G. Friend, Thermophysical Properties of Fluid Systems, in P. J. Linstrom and W. G. Mallard (eds.), *NIST Chemistry WebBook*, NIST Standard Reference Database Number 69, National Institute of Standards and Technology, Gaithersburg MD. Available from: http://webbook.nist.gov

18. T. H. Yen, C. Y. Soong, and P. Y. Tzeng, Hybrid Molecular Dynamics-Continuum Simulation for Nano/Mesoscale Channel Flows, *Microfluid. Nanofluid.*, vol. 3, no. 6, pp. 665–675, 2007.

19. M. P. Allen and D. J. Tildesley, *Computer Simulation of Liquids*, Clarendon Press, Oxford, 1987.

20. J. Liu, S. Y. Chen, X. Nie, and M. O. Robbins, A Continuum–Atomistic Simulation of Heat Transfer in Micro- and Nano-Flows, *J. Comput. Phys.*, vol. 227, no. 1, pp. 279–291, 2007.

21. R. Delgado-Buscalioni and P. V. Coveney, USHER: An Algorithm for Particle Insertion in Dense Fluids, *J. Chem. Phys.*, vol. 119, no. 2, pp. 978–987, 2003.

22. G. S. Grest and K. Kremer, Molecular Dynamics Simulation for Polymers in the Presence of a Heat Bath, *Phys. Rev. A*, vol. 33, no. 5, pp. 3628–3631, 1986.

23. F. Goujon, P. Malfreyt, and D. J. Tildesley, The Gas-Liquid Surface Tension of Argon: A Reconciliation between Experiment and Simulation, *J. Chem. Phys.*, vol. 140, no. 24, pp. 1–6, 2014.

24. G. E. Cossali, M. Marengo, A. Coghe, and S. Zhdanov, The Role of Time in Single Drop Splash on Thin Film, *Exp. Fluids*, vol. 36, no. 6, pp. 888–900, 2004.